

# **A universal chemical-induced tensile strain tuning strategy to boost oxygen-evolving electrocatalysis on perovskite oxides**

Daqin Guan,<sup>1,a)</sup> Jian Zhong,<sup>1</sup> Hengyue Xu,<sup>2</sup> Yu-Cheng Huang,<sup>3</sup> Zhiwei Hu,<sup>4</sup> Bin Chen,<sup>5</sup> Yuan Zhang,<sup>5</sup> Meng Ni,<sup>6</sup> Xiaomin Xu,<sup>7</sup> Wei Zhou,<sup>1</sup> and Zongping Shao<sup>1,7, a)</sup>

## **AFFILIATIONS**

<sup>1</sup>State Key Laboratory of Materials-Oriented Chemical Engineering, College of Chemical Engineering, Nanjing Tech University, Nanjing 211800, China.

<sup>2</sup>State Key Laboratory of Chemical Oncogenomics, Tsinghua Shenzhen International Graduate School, Tsinghua University, Shenzhen 518055, China.

<sup>3</sup>Department of Physics, Tamkang University, 151 Yingzhuan Rd., New Taipei City 25137, Taiwan.

<sup>4</sup>Max-Planck-Institute for Chemical Physics of Solids, Nöthnitzer Str. 40, Dresden 01187, Germany.

<sup>5</sup>Guangdong Provincial Key Laboratory of Deep Earth Sciences and Geothermal Energy Exploitation and Utilization, Institute of Deep Earth Sciences and Green Energy, Shenzhen University, Shenzhen 518060, China.

<sup>6</sup>Department of Building and Real Estate, Research Institute for Sustainable Urban Development (RISUD) and Research Institute for Smart Energy (RISE), The Hong Kong Polytechnic University, Hung Hom, Kowloon 999077, Hong Kong, China.

<sup>7</sup>WA School of Mines: Minerals Energy and Chemical Engineering (WASM-MECE), Curtin University, Perth, WA 6102, Australia.

<sup>a)</sup>**Author to whom correspondence should be address:** [daqinguan1994@gmail.com](mailto:daqinguan1994@gmail.com);  
[shaozp@njtech.edu.cn](mailto:shaozp@njtech.edu.cn)

## Abstract

Exploring effective, facile and universal tuning strategies to optimize material physicochemical properties and catalysis processes is critical for many sustainable energy systems, but still challenging. Herein, we succeed to introduce tensile strain into various perovskites via a facile thermochemical reduction method, which can greatly improve material performance for the bottleneck oxygen-evolving reaction in water electrolysis. As an ideal proof-of-concept, such chemical-induced tensile strain turns hydrophobic  $\text{Ba}_5\text{Co}_{4.17}\text{Fe}_{0.83}\text{O}_{14-\delta}$  perovskite into the hydrophilic one by modulating its solid-liquid tension, contributing to its beneficial adsorption of important hydroxyl reactants as evidenced by fast *operando* spectroscopy. Both surface-sensitive and bulk-sensitive absorption spectra show this strategy introduces oxygen vacancies into the saturated face-sharing Co-O motifs of  $\text{Ba}_5\text{Co}_{4.17}\text{Fe}_{0.83}\text{O}_{14-\delta}$  and transforms such local structure into the unsaturated edge-sharing units with positive charges and enlarged electrochemical active areas, creating a molecular-level hydroxyl pool. Theoretical computations reveal that this strategy well reduces the thermodynamic energy barrier for hydroxyl adsorption, lowers the electronic work function and optimizes the charge/electrostatic potential distribution to facilitate the electron transport between active sites and hydroxyl reactants. Also, this strategy is reliable for other single, double and Ruddlesden-Popper perovskites. We believe this finding will enlighten rational material design and in-depth understanding for many potential applications.

## I. INTRODUCTION

Electrochemical processes are believed to successfully bridge the gap between energy demand and supply in the future, which are changing present production and living.<sup>1</sup> Electrochemical oxygen evolution reaction (OER) plays a key role in many promising sustainable energy devices, such as water electrolysis, fuel cells and rechargeable metal-air batteries.<sup>2</sup> However, these applications all involve the sluggish four-electron OER processes, which require efficient, cost-effective and scalable OER electrocatalysts to lower the reaction energy barrier and accelerate reaction kinetics.<sup>3</sup> Among various noble-metal-free electrocatalyst candidates, perovskite oxides, with merits of abundant elements, low cost, facile synthesis, flexible compositional tunability and large physiochemical property degrees of freedom, have been pushed to the forefront of OER studies.<sup>4</sup> Thus, numerous perovskite families have been developed for catalyzing OER during the past decade.<sup>5</sup> This triggers an important and challenging open question that how to explore a reliable, facile and universal tuning strategy to further enhance the OER performance of various perovskites. Besides, in-depth insights into such strategies will be extremely helpful for the rational design of new electrocatalysts in many potential applications.

Many material tuning strategies have been reported to regulate the information of molecular-level structures, electronic structures and macroscopic physiochemical properties in perovskite-type electrocatalysts. In terms of molecular-level structural information, effective modulation of bond length,<sup>6</sup> bond angle,<sup>7</sup> coordination number<sup>8</sup> and tolerance factor<sup>9</sup> in perovskite lattice can well affect the electrochemical

performance. For electronic structures, the properties of valence,<sup>10</sup> electronegativity,<sup>11</sup> covalency<sup>12</sup> and orbital information (i.e.,  $e_g$  occupation,<sup>2</sup> spin,<sup>13</sup> O  $2p$  band center,<sup>14</sup> band gap<sup>15</sup> and charge-transfer energy<sup>16</sup>) successfully explained the activity trends of perovskites and demonstrated the underlying correlations. Moreover, macroscopic physiochemical properties of perovskites, such as magnetism,<sup>17</sup> conductivity<sup>18</sup> and hydrophilia,<sup>19</sup> are also important to affect their electrochemical catalysis processes. To effectively optimize above properties, numerous perovskites were developed, including delafossite  $ABO_{2-\delta}$ ,<sup>20</sup> single perovskite  $ABO_{3-\delta}$ ,<sup>2</sup> single-layer Ruddlesden-Popper (RP) perovskite  $A_2BO_{4-\delta}$ ,<sup>21</sup> double perovskite  $A_2B_2O_{6-\delta}$ ,<sup>14</sup> double-layer RP perovskite  $A_3B_2O_{7-\delta}$ ,<sup>22</sup> triple perovskite  $A_3B_3O_{9-\delta}$ ,<sup>23</sup> three-layer RP perovskite  $A_4B_3O_{10-\delta}$ ,<sup>24</sup> quadruple perovskite  $A_4B_4O_{12-\delta}$ ,<sup>25</sup> 5H-polytype perovskite  $A_5B_5O_{14-\delta}$ <sup>7</sup> and hexagonal perovskite  $A_8B_4O_{15-\delta}$ ,<sup>26</sup> where A-sites are alkaline/rare-earth metal cations and B-sites are transition-metal cations.

Strain engineering belongs to the structural tuning strategy, which has been widely and successfully applied in noble metals,<sup>27</sup> alloys,<sup>28</sup> simple oxides,<sup>29</sup> layered oxides<sup>30</sup> and layered hydroxides.<sup>31</sup> For perovskite oxides, strain is usually introduced into lattice by complex thin-film growth method, which shows strict requirements in the choice of substrates, perovskites and growth conditions.<sup>32,33</sup> In addition, considering that material features of molecular-level structures, electronic structures and macroscopic physiochemical properties all exert important effects on perovskite performance as mentioned above, we seek to explore a facile, reliable and universal tuning strategy to introduce the strain into perovskite motifs and simultaneously optimize their structural,

electronic structural and macroscopic physiochemical information, aimed at regulating their OER adsorption processes and further boosting their OER performance.

To solve above scientific issues, we successfully introduce the tensile strain into various perovskites and simultaneously regulate their abovementioned physicochemical properties and catalysis processes by a facile, controllable, effective and universal thermochemical reduction method, realizing much-enhanced OER performance of different perovskites. Among various perovskites, we take the view that 1D 5H-polytype  $A_5B_5O_{14-\delta}$  perovskite with large and flexible structural unit is an ideal proof-of-concept to introduce the chemical-induced tensile strain. Therefore, we first apply this strategy on 1D 5H-polytype  $Ba_5Co_{4.17}Fe_{0.83}O_{14-\delta}$  (BCF) perovskite. Combined measurements of solid-liquid contact angle, Fourier transform infrared (FTIR) spectroscopy and fast *operando* X-ray absorption spectroscopy (XAS) show that such chemical-induced tensile strain can well optimize the solid-liquid tension and make hydrophobic BCF tend to adsorb liquid and  $OH^-$  reactants. Multiple XAS techniques offer a molecular-level standpoint that this chemical-induced tensile strain transforms the saturated face-sharing Co-O motifs in BCF to the unsaturated edge-sharing Co-O units with oxygen vacancies, where such unique local structures possess positive charges and large electrochemical active areas and can serve as a molecular-level  $OH^-$  pool. Further density functional theory (DFT) calculations demonstrate that this transition effectively lowers the  $OH^-$  adsorption energy and the electronic work function as well as regulates the charge/electrostatic potential distribution, which can greatly promote the OER electron transport and the OER performance. Specifically, the overpotential at  $10 \text{ mA cm}_{\text{disk}}^{-2}$  of

BCF under this chemical-induced tensile strain tuning strategy dramatically reduces by 83 mV as compared with the pristine counterpart. Besides, the intrinsic and mass OER current densities at overpotentials of 370 mV and 350 mV for the modified BCF are  $\sim 4.6$  and  $\sim 5.7$  times that of the initial counterpart, which even surpass almost all the cobalt-based perovskite oxides reported so far. It is worth mentioning that the modified BCF can steadily catalyze OER at  $10 \text{ mA cm}_{\text{disk}}^{-2}$  for even 150 h. The universality of this tuning strategy is further verified by other single, double and RP-type perovskites. We believe that this work will offer meaningful and systematic insights into the rational material design and in-depth understanding for many emerging energy and environmental applications.

## II. INTRODUCTION OF CHEMICAL-INDUCED TENSILE STRAIN

We first introduced the tensile strain into BCF perovskite by reducing pristine BCF under different temperatures in  $\text{NH}_3$  atmosphere [**Fig. 1(a)**]. As shown in **Fig. 1(a)** left, the structural unit of 1D 5H-polytype BCF perovskite is composed of four groups of face-shared octahedrons and two corner-shared tetrahedrons along  $c$  axis,<sup>34</sup> which is confirmed by our X-ray diffraction (XRD) refinement results [**Fig. 1(b)** and **Table SI**]. The samples reduced under 200 °C, 325 °C, 335 °C, 400 °C and 450 °C in  $\text{NH}_3$  atmosphere are denoted as BCF-200, BCF-325, BCF-335, BCF-400 and BCF-450, respectively. We can observe that the main XRD peak shifts to lower degrees from BCF to BCF-200 and further to BCF-325 (**Fig. S1**), indicating that the structural unit of BCF enlarges with higher reduction temperatures in  $\text{NH}_3$  atmosphere. This can be ascribed

to the appearance of chemical-induced tensile strain into perovskite lattice. The BCF perovskite structure is destroyed when the temperature is above 325 °C (**Fig. S1**), which means BCF-325 perovskite should exhibit the largest chemical-induced tensile strain in this system.

To study the chemical-induced tensile strain in our perovskites, we combined XRD refinement, Williamson-Hall analysis, Raman, high-resolution transmission electron microscopy (HRTEM) and strain mapping to compare the strain in BCF-325 and pristine BCF. As shown in **Fig. 1(b)** and **Table SI**, BCF-325 and BCF both exhibit the  $P-3m1$  space group while the cell volume of BCF-325 ( $339.4 \text{ \AA}^3$ ) is larger than that of BCF ( $337.0 \text{ \AA}^3$ ), implying the greater tensile strain in BCF-325 lattice. Moreover, we conducted the Williamson-Hall analysis of two XRD patterns following the equation of  $\beta\cos\theta = k\lambda/D + 4\epsilon\sin\theta$ , where  $k = 0.94$  and  $\beta$ ,  $\theta$ ,  $\lambda$ ,  $D$  and  $\epsilon$  stand for the peak width at half-maximum intensity, diffraction position, wavelength of radiation, particle size and strain component, respectively.<sup>31,35</sup> We can obtain the strain  $\epsilon$  in BCF and BCF-325 from the slope by plotting  $\beta\cos\theta$  versus  $4\sin\theta$ . As revealed in **Fig. 1(c)**,  $\epsilon$  of BCF-325 is much more positive than that of pristine BCF, confirming the larger tensile strain in BCF-325. Besides, we observed relatively lower Raman peak positions on BCF-325 as compared with BCF [**Fig. 1(d)**], which could also be attributed to the existence of large tensile strain in BCF-325.<sup>31,36</sup> Due to the appearance of tensile strain in BCF-325, the interplanar distance of the (103) plane increases from 3.10 Å in BCF to 3.16 Å in BCF-325 [**Figs. 1(e)** and **1(f)**]. More directly, the strain mapping images of BCF and BCF-325 obviously verify the larger tensile strain in BCF-325 [**Figs. 1(g)** and **1(h)**], where

the regions from yellow to red and from blue to green represent the tensile and compressive strain, respectively.<sup>37,38</sup> It is worth noting that the elements in BCF-325 are homogeneously distributed and N element is absent in BCF-325 as revealed in the results of scanning electron microscopy (SEM) elemental mapping images [Fig. 1(i)] and N 1s X-ray photoelectron spectroscopy (XPS) spectra (Fig. S2).

**FIG. 1.** Introduction of tensile strain. (a) A schematic diagram of introducing tensile strain into  $A_5B_5O_{14}$  perovskite structure (namely BCF) by chemical reduction under a certain temperature in  $NH_3$  atmosphere. (b) XRD refinement results of BCF and BCF-325. (c) Williamson-Hall analysis of corresponding XRD patterns. (d) Raman spectra of BCF and BCF-325. HRTEM images of (e) BCF and (f) BCF-325. Scale bar is 5 nm. Strain mapping images of (g) BCF and (h) BCF-325. (i) SEM elemental mapping images for BCF-325, where the N elements are from the conductive tapes. Scale bar is 1  $\mu m$ .

### III. OER PERFORMANCE AND ADSORPTION ABILITY

Next, we followed the traditional protocols of OER measurements<sup>7,26</sup> in 0.1 M KOH on a three-electrode configuration to investigate the effects of chemical-induced tensile strain on OER performance. The electrode potentials were *iR*-corrected and referenced to the reversible hydrogen electrode (RHE, Fig. S3). As presented in Fig. S4 and Fig. 2(a), BCF-325 perovskite with the largest tensile strain exhibits the best electrode OER activity among all synthesized samples. Specifically, the overpotential

at  $10 \text{ mA cm}_{\text{disk}}^{-2}$  for BCF-325 (335 mV) is much lower than that for pristine BCF (418 mV) and BCF-450 (370 mV) with destroyed structure [Fig. 2(a)]. Considering that the particle size of BCF decreases with increasing reduction temperatures (Fig. S5), we also normalized the OER activities to the Brunauer-Emmett-Teller (BET) surface areas of our samples (Table SII). As depicted in Fig. 2(b), the intrinsic current density at 370 mV overpotential for BCF-325 ( $8.51 \text{ mA cm}_{\text{oxide}}^{-2}$ ) is  $\sim 4.6$  and  $\sim 2.8$  times that for BCF ( $1.86 \text{ mA cm}_{\text{oxide}}^{-2}$ ) and BCF-450 ( $3.03 \text{ mA cm}_{\text{oxide}}^{-2}$ ), respectively. Moreover, the electrode mass activity at 350 mV overpotential for BCF-325 ( $62.61 \text{ mA mg}_{\text{oxide}}^{-1}$ ) is  $\sim 5.7$  and  $\sim 2.6$  times higher than BCF ( $10.90 \text{ mA mg}_{\text{oxide}}^{-1}$ ) and BCF-450 ( $23.66 \text{ mA mg}_{\text{oxide}}^{-1}$ ), respectively [Fig. 2(c)]. It is also worth mentioning that above OER activities achieved by BCF-325 with the maximal chemical-induced tensile strain are superior to most recently reported cobalt-based perovskites (Table SIII), corroborating the efficiency of chemical-induced tensile strain tuning strategy. In addition to the OER activity, BCF-325 also delivers a robust OER stability at  $10 \text{ mA cm}_{\text{disk}}^{-2}$  for 150 h, which is much more stable than BCF-450 [Fig. 2(d)].

From the standpoint of reaction adsorption processes, we attempted to explore the origins of the activity difference between BCF and BCF-325. Considering that the adsorption of  $\text{OH}^-$  reactants is the first and important step for alkaline OER,<sup>3,39</sup> we performed solid-liquid contact angle, FTIR spectroscopy and fast *operando* XAS measurements to experimentally compare the adsorption ability of BCF and BCF-325. As shown in Fig. 2(e), the solid-liquid contact angles for BCF and BCF-325 are  $125^\circ$  and  $32^\circ$ , respectively. This means that pristine BCF is hydrophobic and becomes

hydrophilic after introducing chemical-induced tensile strain into lattice. The relationship between tension and contact angle can be well demonstrated by the Young equation, namely  $\cos\theta = (\sigma_{SG} - \sigma_{SL})/\sigma_{LG}$ ,<sup>40</sup> where  $\theta$ ,  $\sigma_{SG}$ ,  $\sigma_{SL}$  and  $\sigma_{LG}$  stand for the contact angle, solid-gas tension, solid-liquid tension and liquid-gas tension, respectively. The appearance of tensile strain in BCF-325 may optimize its solid-liquid tension and endow it with the hydrophilic feature, which may favor its adsorption of OH<sup>-</sup> reactants in liquid. To prove above point, we measured the FTIR spectra of BCF and BCF-325 before and after immersing in 0.1 M KOH. As demonstrated in **Fig. 2(f)**, BCF-325 shows stronger OH<sup>-</sup> adsorption bands (at  $\sim 3448\text{ cm}^{-1}$ )<sup>41,42</sup> as compared with BCF before and after immersing in 0.1 M KOH, confirming the better OH<sup>-</sup> adsorption ability of BCF-325.

Furthermore, we applied the fast *operando* Co-K XAS technique in transmission mode to track the adsorption behaviors of BCF and BCF-325 during OER, where the enhanced intensity of the first Co-O shell in *operando* Co-K extended X-ray absorption fine structure (EXAFS) spectra can be ascribed to the adsorption of OH<sup>-</sup> species as convinced by literatures.<sup>39,43</sup> Compared with pristine BCF, the intensity increase of Co-O shell for BCF-325 in *operando* Co-K EXAFS spectra is obviously larger [**Fig. 2(g)**], verifying the active behavior of OH<sup>-</sup> adsorption on BCF-325 during OER. Systematic theoretical insights into the OH<sup>-</sup> adsorption step on BCF and BCF-325 will be given after the discussions of the effects on material electronic structures and local structures below.

**FIG. 2.** OER performance and adsorption ability. (a) Electrode OER activities, (b)

electrode intrinsic OER performance and (c) electrode mass OER curves of BCF, BCF-325 and BCF-450. (d) OER stability of BCF, BCF-325 and BCF-450 at  $10 \text{ mA cm}_{\text{disk}}^{-2}$  on carbon paper. (e) Solid-liquid contact angles of BCF and BCF-325. (f) FTIR spectra of BCF and BCF-325 before and after immersing in liquid. (g) Fast *operando* Co-K EXAFS spectra for BCF and BCF-325. All the measurements were conducted in 0.1 M KOH at 25 °C.

#### IV. ELECTRONIC STRUCTURE AND LOCAL STRUCTURE

In addition to the crystal structure, we have to glean the detailed information of electronic structure and local structure in pristine BCF and strained BCF-325, which are also important for the modeling in DFT calculations. Soft and hard XAS spectra are two advanced and effective techniques to extract the detailed information of material electronic structures and local structures.<sup>39,44,45</sup> To obtain the properties of valence, covalence, oxygen vacancy and coordination in pristine BCF and strained BCF-325, we measured the soft XAS spectra in total electron yield (TEY) and fluorescence yield (FY) modes, where TEY and FY modes are sensitive to material surface ( $\sim 5 \text{ nm}$  depth) and bulk ( $\sim 200 \text{ nm}$  depth) information, respectively.<sup>11,39,46</sup>

As revealed in **Fig. 3(a)** top, the Co- $L_3$  peak in TEY mode shifts to higher energy positions from pure  $\text{Co}^{2+}$  to  $\text{Co}^{3+46}$  and further to  $\text{Co}^{4+47}$  standard references. We can observe that the Co- $L_3$  peaks of pristine BCF and strained BCF-325 both locate between the  $\text{Co}^{3+}$  and  $\text{Co}^{4+}$  standard references, showing their mixed Co valence of  $\text{Co}^{3+}$  and  $\text{Co}^{4+}$ . Compared with pristine BCF, the Co- $L_3$  peak of strained BCF-325 moves to

relatively lower energy position [**Fig. 3(a)** top], indicating that the Co valence of strained BCF-325 is lower than that of pristine BCF. According to the spectral feature, we can estimate the Co valence states for strained BCF-325 and pristine BCF are  $\sim 3.1+$  and  $\sim 3.4+$ , respectively. These results are also in line with the findings of bulk-sensitive Co- $L_3$  XAS spectra in FY mode for pristine BCF and strained BCF-325 [**Fig. 3(a)** bottom]. The Fe- $L_3$  XAS spectra in TEY mode show that the  $e_g$  peak of strained BCF-325 shifts to lower energy region and its intensity of  $t_{2g}$  peak weakens as compared to pristine BCF (**Fig. S6**), which suggests that the Fe valence of strained BCF-325 is smaller than pristine BCF and the Fe-O coordination number is reduced in strained BCF-325.<sup>48,49</sup> The conclusion of the reduced Fe-O coordination number in BCF-325 can be supported by comparing the intensity of  $t_{2g}$  peaks for  $\text{Fe}_2\text{O}_3$  with pure  $\text{FeO}_6$  coordination and  $\text{YBaCo}_3\text{FeO}_7$  with pure  $\text{FeO}_4$  coordination in **Fig. S6**. Owing to the lower Co and Fe valence states in strained BCF-325, the consumption of  $\text{Na}_2\text{S}_2\text{O}_3$  solutions on strained BCF-325 for complete iodometric titration is less than that on pristine BCF (**Fig. S7**).

Due to the requirement of charge balance in perovskites, strained BCF-325 with lower Co and Fe valence states should possess less lattice oxygen sites or more oxygen vacancies than pristine BCF with relatively higher Co and Fe valence states in theory. As depicted in **Fig. S8**, strained BCF-325 indeed exhibits a lower peak intensity of lattice oxygen sites at  $\sim 529$  eV in O 1s XPS spectra<sup>7,41</sup> as compared to pristine BCF, corroborating the less lattice oxygen sites or more oxygen vacancies in strained BCF-325. Furthermore, we performed O-K XAS measurements for our samples, where this

technique is very instrumental for the analysis of the covalence between transition metals (TM) and lattice oxygen sites in oxides.<sup>10,11,46,50</sup> In the O-*K* XAS spectrum, the pre-edge peak below ~531 eV stands for the TM 3*d*-O 2*p* hybridization in oxides and this peak shifts to lower energy regions and gains spectral weight with increasing TM valence and enhanced TM-O covalence.<sup>10,11,46,50</sup> As shown in **Fig. 3(b)**, the O-*K* pre-edge peaks in TEY (top) and FY (bottom) modes for strained BCF-325 move to higher energy positions and reduce peak weight as compared with those for pristine BCF, demonstrating the lower TM valence, more oxygen vacancies and reduced TM-O covalence in strained BCF-325. These findings accord well with above results.

To study the variations of the local structures in pristine BCF after introducing chemical-induced tensile strain into its lattice, we conducted hard XAS measurements in the transmission mode, where Co-*K* X-ray absorption near-edge structure (XANES) and EXAFS spectra can further check the Co valence and analyze material local structure, respectively.<sup>39,51,52</sup> For the Co-*K* XANES spectra, it was reported that the normalized absorption position of 0.7~0.8 shifts to lower energy ranges with decreasing Co valence.<sup>7,39,52</sup> Briefly, the information at the normalized absorption position of 0~0.6 is greatly affected by the inter-site screening effects, which is strongly determined by Co-O-Co networks rather than Co valence.<sup>53</sup> Therefore, we choose the normalized absorption position of 0.7~0.8 in the Co-*K* XANES spectra for the analysis of Co valence. We find that the normalized Co-*K* XANES absorption position of 0.7~0.8 for strained BCF-325 moves to lower energy positions relative to pristine BCF [**Fig. 3(c)**], verifying the lower Co valence of strained BCF-325. The Co-*K* EXAFS spectra in **Fig.**

**3(d)** reveal that the intensity of Co-O shell (at  $\sim 1.43$  Å) for strained BCF-325 decreases and shifts to higher positions as compared with pristine BCF, which can be attributed to the lower Co valence and more oxygen vacancies in strained BCF-325.<sup>7,39</sup> Interestingly, we can observe that the face-sharing Co-Co/Fe motifs (at  $\sim 2.22$  Å)<sup>7,43</sup> in pristine BCF transform to the edge-sharing Co-Co/Fe units (at  $\sim 2.40$  Å)<sup>39,43</sup> in strained BCF-325 [**Fig. 3(d)**]. The existence of face-sharing Co-Co/Fe motifs with three couples of combined bonds in BCF [**Fig. 3(e)**] and edge-sharing Co-Co/Fe units with two couples of shared bonds in BCF-325 [**Fig. 3(e)**] contribute to their durable OER stability [**Fig. 2(d)**], which are in line with prior findings.<sup>7,39,46</sup> It is also worth mentioning that the Co-Co metal shell (at  $\sim 2.18$  Å) is absent in strained BCF-325 as compared to Co foil reference [**Fig. 3(d)**], ruling out the possible Co exsolution from the lattice.

We can conclude from above analysis of electronic structures and local structures in pristine BCF and strained BCF-325 that chemical-induced tensile strain induces oxygen vacancies into the saturated face-sharing Co-O motifs of pristine BCF, leading to its decreased Co valence, reduced TM-O covalence and transformation into the unsaturated edge-sharing Co-O units with exposed positive Co ions [**Fig. 3(e)**]. These variations can greatly enlarge the electrochemical active areas of strained BCF-325 [**Figs. S9(a-c)**] to accelerate the OER processes. It is worth noting that the OER performance normalized to the value of electrochemical active surface area (ECSA) for strained BCF-325 is still superior to pristine BCF [**Fig. S9d**]. To offer an insight into the distribution of OH<sup>-</sup> reactants with negative charges on strained BCF-325 with positive charges, we utilized numerical simulations and observed a pool-like distribution [**Fig.**

3(f)], where the OH<sup>-</sup> concentration near the active sites is larger than that in the bulk solution. We will further understand the OH<sup>-</sup> adsorption step on pristine BCF and strained BCF-325 from a molecular-level standpoint via theoretical DFT calculations below.

**FIG. 3.** Electronic structure and local structure. (a) Soft XAS spectra of BCF and BCF-325 at Co- $L_3$  edge in TEY (top) and FY (bottom) modes, where CoO, Li<sub>2</sub>Co<sub>2</sub>O<sub>4</sub> and BaCoO<sub>3</sub> single crystals were used as the references for pure Co<sup>2+</sup>, Co<sup>3+</sup> and Co<sup>4+</sup>, respectively. (b) Soft XAS spectra of BCF and BCF-325 at O- $K$  edge in TEY (top) and FY (bottom) modes. (c) The Co- $K$  XANES and (d) corresponding Co- $K$  EXAFS spectra in transmission mode for BCF and BCF-325. (e) A schematic diagram of the transformation from saturated face-sharing motifs in BCF to unsaturated edge-sharing units in BCF-325 by the chemical-induced tensile strain. (f) Numerical simulations of the distribution of OH<sup>-</sup> reactants with negative charges on the exposed active sites with positive charges. The colour bar represents the OH<sup>-</sup> concentration.

## V. THEORETICAL INSIGHTS IN MOLECULAR LEVEL

Based on above structural, electronic structural and local structural results, we can further construct models for DFT calculations to have insights into the OH<sup>-</sup> adsorption step on pristine BCF and strained BCF-325 from a molecular-level standpoint. Specifically, the computations of thermodynamic energy barrier, electronic work function and charge/electrostatic potential distribution were performed to systematically

and theoretically understand the OH<sup>-</sup> adsorption step on pristine BCF and strained BCF-325. As depicted in **Fig. 4(a)**, strained BCF-325 shows a much lower thermodynamic energy barrier of OH<sup>-</sup> adsorption step (-3.38 eV) than pristine BCF (-2.37 eV). This means strained BCF-325 tends to adsorb important OH<sup>-</sup> reactants in theory, which is well in line with our experimental findings [**Figs. 2(e-g)**]. The favorable adsorption of important OH<sup>-</sup> reactants on strained BCF-325 will accelerate its OER processes and promote its OER activity.

To investigate the electronic transfer in the OH<sup>-</sup> adsorption step on pristine BCF (denoted as BCF-OH) and strained BCF-325 (denoted as BCF-325-OH), we calculated the electronic work function for our samples. Electronic work function represents the minimum thermodynamic work needed for an electron to escape from material lattice to a point outside material surface,<sup>54</sup> where the value of work function ( $\Phi$ ) can be calculated as the electrostatic potential difference between vacuum level and Fermi level.<sup>54</sup> It was reported that a lower work function is instrumental to enhance the electronic transport between catalyst and reactants in liquid.<sup>54</sup> As depicted in **Fig. 4(b)**, BCF-325-OH (5.005 eV) exhibits a lower  $\Phi$  value as compared with BCF-OH (5.134 eV), demonstrating the faster electron transfer between strained BCF-325 and OH<sup>-</sup> reactants. Our measured electrochemical impedance spectroscopy (EIS) results further prove this point experimentally (**Fig. S10**).

Also, we calculated the charge distribution of BCF-OH and BCF-325-OH. As presented in **Figs. 4(c)** and **4(d)**, the yellow and blue regions stand for the electron inflow and outflow, respectively.<sup>55</sup> We can clearly observe that the yellow region around

the adsorbed OH<sup>-</sup> in the charge density difference between BCF-325-OH and BCF-325 [Fig. 4(d)] is larger than that between BCF-OH and BCF [Fig. 4(c)], namely the electron inflow into the adsorbed OH<sup>-</sup> in BCF-325-OH is more than that in BCF-OH. This can also be reflected by the more negative oxygen atomic charge of OH<sup>-</sup> in BCF-325-OH [-1.48 e in Fig. 4(d)] as compared with BCF-OH [-0.88 e in Fig. 4(c)]. The Co atomic charges of active Co sites in BCF-325-OH [+1.55 e and +1.56 e in Fig. 4(d)] are more positive than those in BCF-OH [+1.53 e and +1.53 e in Fig. 4(c)], implying the more electron outflow from the active Co sites in BCF-325-OH.<sup>56</sup> The favorable electron outflow from the active Co sites to the adsorbed OH<sup>-</sup> in BCF-325-OH creates a fast pathway for the electron transport between active Co sites and OH<sup>-</sup> reactants, which accords well with above theoretical and experimental findings.

Moreover, we compared the electrostatic potential distribution of pristine BCF, BCF-OH, strained BCF-325 and BCF-325-OH by calculating their electrostatic potential maps, where the positive and negative electrostatic potential can serve as electron receptor and donor sites, respectively.<sup>57,58</sup> As presented in Figs. 4(e-h), the electrostatic potentials around the isosurfaces of Co active sites for strained BCF-325 [black dotted circle in Fig. 4(g)] and pristine BCF [black dotted circle in Fig. 4(e)] before the adsorption of OH<sup>-</sup> reactants are positive and negative, respectively. This indicates that the unsaturated Co active sites of strained BCF-325 can serve as the electron receptor sites to promote the adsorption of OH<sup>-</sup> reactants due to the requirement of charge balance. After adsorbing OH<sup>-</sup> reactants, the electrostatic potentials are both redistributed around the isosurfaces of Co active sites for BCF-325-OH [Fig. 4(h)] and

BCF-OH [Fig. 4(f)].

From a molecular-level standpoint, we can conclude from above DFT calculation results that the unsaturated Co-O edge-sharing motifs in strained BCF-325 show optimized thermodynamic energy barrier, electronic work function and charge/electrostatic potential distribution to create an ideal molecular-level pool for OH<sup>-</sup> adsorption.

**FIG. 4.** DFT calculations. (a) The calculated OH<sup>-</sup> adsorption energy for BCF and BCF-325. (b) The work function for BCF-OH (top) and BCF-325-OH (bottom). (c) The charge density difference between BCF-OH and BCF as well as calculated atomic charge. (d) The charge density difference between BCF-325-OH and BCF-325 as well as calculated atomic charge. The calculated electron-density isosurface for (e) BCF, (f) BCF-OH, (g) BCF-325 and (h) BCF-325-OH. The colour bar stands for the electrostatic potential scale.

## VI. UNIVERSALITY OF THE STRATEGY

Furthermore, to investigate the universality of our chemical-induced tensile strain tuning strategy, we applied our strategy in other typical single [ABO<sub>3-δ</sub> in Fig. 5(a)], double [AA'B<sub>2</sub>O<sub>6-δ</sub> in Fig. 5(b)] and RP-type [A<sub>2</sub>BO<sub>4-δ</sub> in Fig. 5(c)] perovskite oxides. Specifically, single perovskite Ba<sub>0.5</sub>Sr<sub>0.5</sub>Co<sub>0.8</sub>Fe<sub>0.2</sub>O<sub>3-δ</sub> (BSCF), double perovskite PrBaCo<sub>2</sub>O<sub>6-δ</sub> (PBC) and RP-type perovskite La<sub>0.5</sub>Sr<sub>1.5</sub>Co<sub>0.8</sub>Fe<sub>0.2</sub>O<sub>4-δ</sub> (LSCF) were studied. Corresponding XRD refinement results show that BSCF, PBC and LSCF are all pure-

phase and exhibit space group of  $Pm-3m$ ,  $P4/mmm$  and  $I4/mmm$  [Figs. S11(a-c) and Table SI], respectively. Similarly, we reduced the BSCF, PBC and LSCF powders under different temperatures in  $NH_3$  atmosphere and obtained BSCF-400, BSCF-700, PBC-400, PBC-700, LSCF-450 and LSCF-800. As presented in Figs. 5(d-f), the main XRD peaks of BSCF-400, PBC-400 and LSCF-450 move to lower degree regions as compared with pristine BSCF, PBC and LSCF, respectively, indicating the enlarged structural units triggered by the existence of tensile strain in BSCF-400, PBC-400 and LSCF-450. Besides, we can observe that the perovskite structures were destroyed for BSCF-700, PBC-700 and LSCF-800 samples. As expected, strained BSCF-400, PBC-400 and LSCF-450 exhibit the best OER performance in their respective systems [Figs. 5(g-i)]. These results strongly corroborate the universality and reliability of our strategy.

**FIG. 5.** Universality of the chemical-induced tensile strain tuning strategy in other typical perovskite systems. Introducing chemical-induced tensile strain into (a) single perovskite  $ABO_3$  (b) double perovskite  $A_2B_2O_6$  and (c) Ruddlesden-Popper perovskite  $A_2BO_4$  structures. XRD spectra of (d) single perovskite BSCF, BSCF-400, BSCF-700, (e) double perovskite PBC, PBC-400, PBC-700, (f) Ruddlesden-Popper perovskite LSCF, LSCF-450 and LSCF-800, where the suffixes represent the values of different temperatures treated in  $NH_3$  atmosphere. Electrode OER activities of (g) single perovskite BSCF, BSCF-400, BSCF-700, (h) double perovskite PBC, PBC-400, PBC-700, (i) Ruddlesden-Popper perovskite LSCF, LSCF-450 and LSCF-800 in 0.1 M KOH at 25 °C.

## VII. CONCLUSIONS

In this work, we report a facile, effective and universal chemical-induced tensile strain tuning strategy to simultaneously and successfully optimize the structural, electronic structural and macroscopic physiochemical properties of perovskite oxides, which can further strengthen material adsorption capability for important reactants and distinctly improve the OER performance. Specifically, the proof-of-concept strained BCF-325 perovskite shows a much-reduced overpotential at  $10 \text{ mA cm}_{\text{disk}}^{-2}$  and its intrinsic and mass OER activities at overpotentials of 370 mV and 350 mV are  $\sim 4.6$  and  $\sim 5.7$  times that of the pristine counterpart, which are superior to almost all the advanced cobalt-based perovskites reported so far. Besides, strained BCF-325 delivers a stable OER operation at  $10 \text{ mA cm}_{\text{disk}}^{-2}$  for 150 h. By combining various advanced characterization techniques, we have given in-depth insights into the positive effects triggered by this unifying strategy on material physicochemical properties and adsorption capabilities. Further numerical simulations and DFT calculations offer theoretical understandings on the adsorption of important  $\text{OH}^-$  reactants for strained BCF-325. Also, this strategy is applicable for other single, double and RP-type perovskites. It is worth mentioning that this facile thermochemical reduction method may be universal by using other reductive atmosphere (such as  $\text{H}_2$ , Ar and  $\text{N}_2$ ) under different temperatures. We anticipate that our facile, effective, unifying and universal material tuning strategy can be used to optimize other catalyst systems for a wide range of reactions and applications.

## VIII. METHODS

### A. Material Synthesis

All the pristine pure-phase BCF, BSCF, PBC and LSCF perovskite oxides were fabricated by a traditional sol-gel method.<sup>7,10</sup> In terms of the synthesis of BCF, stoichiometric amounts of  $\text{Fe}(\text{NO}_3)_3 \cdot 9\text{H}_2\text{O}$ ,  $\text{Co}(\text{NO}_3)_2 \cdot 6\text{H}_2\text{O}$  and  $\text{Ba}(\text{NO}_3)_2$  were dissolved in water. Then, citric acid (CA) and ethylenediaminetetraacetic acid (EDTA) were added with a molar ratio of 2:1:1 for CA/EDTA/total metal ions. Ammonium hydroxide solution was used to tune the pH of mixed solution to a neutral or near-neutral value. The transparent gel was obtained by continuously heating and stirring the mixed solution. The gel was then heated at  $\sim 200$  °C for over 5 h to produce the black solid precursor. The sintered precursor under 1000 °C for 10 h in air finally yielded the BCF perovskite powder. BSCF, PBC and LSCF perovskite powders were obtained through the same procedures. Samples with chemical-induced tensile strain and destroyed structures were obtained by reducing respective pristine perovskite powders under different temperatures in  $\text{NH}_3$  atmosphere for 10 h.

### B. Characterizations

XRD spectra were performed on a Rigaku Smartlab diffractometer with a wavelength of 1.5418 Å for Cu radiation. XRD refinements were conducted by using Topas-4.2 software. Raman results were obtained on a HR800 UV microspectrometer (Jobin Yvon). HRTEM images were measured on a JEM-2100F microscope (JEOL).

Strain mapping images were revealed by the geometric phase analysis. SEM was taken on an S-4800 microscope (HITACHI). XPS was carried on a PHI5000 VersaProbe spectrometer. BET results were extracted from a Quantachrome Autosorb-iQ<sub>3</sub> equipment. Solid-liquid contact was recorded on a DROPMETER A100P instrument (MAIST). FTIR spectra were characterized on a NicoletNexus 470 spectrophotometer (THERMO). Hard and soft XAS spectra were collected at TPS BL 44A and TLS BL 20A of NSRRC in Taiwan, respectively. The *ex-situ* hard XAS spectra were collected in transmission model while the soft XAS spectra were obtained by using TEY and FY modes. The Co foil was used and measured simultaneously for the energy calibration of Co-K XAS spectra. The CoO, Fe<sub>2</sub>O<sub>3</sub> and NiO single crystals were utilized and measured simultaneously to calibrate the energy of Co-L<sub>3</sub>, Fe-L<sub>3</sub> and O-K spectra, respectively. Fast *operando* hard XAS measurements in transmission model were realized at TPS BL 44A with a speed of 120 spectra within 1 min. The sample was prepared on the carbon paper and 5 wt% Nafion solution was used as a binder. A graphite rod and an Ag/AgCl were utilized as the counter and reference electrodes, respectively. The XANES and EXAFS data were analyzed by the ATHENA software packages.<sup>59</sup>

### **C. Electrochemical Measurements**

The OER tests were performed on an SP300 work station with a three-electrode configuration (Pine Research Instrumentation) in O<sub>2</sub>-saturated 0.1 M KOH solutions, where a glassy carbon electrode, a graphite rod and an Ag/AgCl served as the working, counter and reference electrodes, respectively. The working electrode was prepared by

dispersing a 5  $\mu\text{L}$  catalyst ink. The catalyst ink was obtained by dispersing 10 mg perovskite powders and 10 mg carbon black into 1 mL absolute ethanol and 0.1 mL 5 wt% Nafion solution. The mixture was then under mild sonication to form a homogeneous catalyst ink. The calibration of Ag/AgCl reference electrode to the RHE scale was in line with the literatures.<sup>7,39</sup> EIS was measured from 100 kHz to 0.01 Hz under an AC voltage.

#### **D. Theoretical Calculations**

All the DFT calculations were carried on the Vienna Ab initio Simulation Package (VASP) by using spin-polarized DFT with the Hubbard model (DFT + U).<sup>60,61</sup> The projector augmented-wave method and the Perdew-Burke-Ernzerhof exchange-correlation functional were applied.<sup>62,63</sup> For a better description of Co 3*d* electrons, the effective U value was set to 3.5 eV.<sup>64</sup> A kinetic energy cut-off of 500 eV was used. The (110) surface was chosen for adsorption energy computations. The convergence criteria and the electronic structure iteration were 0.02 eV  $\text{\AA}^{-1}$  and  $10^{-5}$  eV, respectively. All the slabbed models possessed three atomic layers and a vacuum spacing of  $\approx 15$   $\text{\AA}$  sampled by a  $2 \times 3 \times 1$  Monkhorst-Pack k-point mesh. The DFT-D3 method with Becke-Jonson damping was adopted to consider the van der Waals correction.<sup>65,66</sup> For an accurate electrostatic potential, the DFT calculation was modified with the dipole correction<sup>67</sup> in the Z-direction. The electron-density isosurface and the charge density difference were plotted at 0.002 and 0.01 e bohr<sup>-3</sup>, respectively. The numerical simulation of the OH<sup>-</sup> concentration in the solution was driven by the surface charge accumulation and

performed based on the classical diffusion double layer model. Nernst-Planck-Poisson equations were applied for the transportation of diluted diffusion and charge.

## **SUPPLEMENTARY MATERIAL**

The supplementary material includes captions for supporting Figs. S1-S11 and Table SI-SIII.

## **AUTHOR CONTRIBUTIONS**

D.G., J.Z., H.X. and Y.H. contributed equally to this study. D.G. conceived the idea and designed the whole subject. Z.S. offered financial supports and supervised the subject. J.Z. and D.G. fabricated all the samples and conducted the electrochemical measurements. J.Z. performed XRD, Raman, SEM, solid-liquid contact, FTIR and iodometric titration. D.G. conducted XRD refinement and *operando* hard XAS spectra. Y.H. measured all the *ex-situ* hard and soft XAS data. W.Z. offered the access to Topas-4.2 software and Z.H. was involved in the analysis of hard/soft XAS spectra. D.G. analyzed all the experimental results. X.X. was involved in the analysis of structural information and helped improve the English. H.X. performed all the DFT calculations. H.X. and D.G. analyzed the DFT results. B.C. performed the numerical simulations and Y.Z. and M.N. were involved in the analysis of numerical results. D.G. drafted the manuscript and all the other coauthors helped improve the manuscript.

## **ACKNOWLEDGEMENTS**

This work was financially supported by National Natural Science Foundation of China of Nos. 21706129, 21576135 and 21878158. The authors also acknowledged the support from the Max Planck-POSTECH-Hsinchu Center for Complex Phase Materials. M.N. would like to thank the funding support from the Project of Strategic Importance Scheme (Project ID: P0035168; Work Programme: ZE1S), The Hong Kong Polytechnic University, Hong Kong, China.

## **DATA AVAILABILITY STATEMENT**

The data that support the findings of this study are available within the article and its supplementary material.

## **REFERENCES**

- <sup>1</sup>Z.W. Seh, J. Kibsgaard, C.F. Dickens, I. Chorkendorff, J.K. Nørskov, and T.F. Jaramillo, “Combining theory and experiment in electrocatalysis: insights into materials design,” *Science* **355**, eaad4998 (2017).
- <sup>2</sup>J. Suntivich, K.J. May, H.A. Gasteiger, J.B. Goodenough, and Y. Shao-Horn, “A perovskite oxide optimized for oxygen evolution catalysis from molecular orbital principles,” *Science* **334**, 1383-1385 (2011).
- <sup>3</sup>N.T. Suen, S.F. Hung, Q. Quan, N. Zhang, Y.J. Xu, and H.M. Chen, “Electrocatalysis for the oxygen evolution reaction: recent development and future perspectives,” *Chem. Soc. Rev.* **46**, 337-365 (2017).
- <sup>4</sup>J. Hwang, R.R. Rao, L. Giordano, Y. Katayama, Y. Yu, and Y. Shao-Horn, “Perovskites

in catalysis and electrocatalysis,” *Science* **358**, 751-756 (2017).

<sup>5</sup>W. Yin, B. Weng, J. Ge, Q. Sun, Z. Li, and Y. Yan, “Oxide perovskites, double perovskites and derivatives for electrocatalysis, photocatalysis, and photovoltaics,” *Energy Environ. Sci.* **12**, 442-462 (2019).

<sup>6</sup>H. Li, Y. Chen, S. Xi, J. Wang, S. Sun, Y. Sun, Y. Du, and Z.J. Xu, “Degree of geometric tilting determines the activity of FeO<sub>6</sub> octahedra for water oxidation,” *Chem. Mater.* **30**, 4313-4320 (2018).

<sup>7</sup>D. Guan, K. Zhang, Z. Hu, X. Wu, J.L. Chen, C.W. Pao, Y. Guo, W. Zhou, and Z. Shao, “Exceptionally robust face-sharing motifs enable efficient and durable water oxidation,” *Adv. Mater.* **33**, 2103392 (2021).

<sup>8</sup>A. Grimaud, C.E. Carlton, M. Risch, W.T. Hong, K.J. May, and Y. Shao-Horn, “Oxygen evolution activity and stability of Ba<sub>6</sub>Mn<sub>5</sub>O<sub>16</sub>, Sr<sub>4</sub>Mn<sub>2</sub>CoO<sub>9</sub>, and Sr<sub>6</sub>Co<sub>5</sub>O<sub>15</sub>: the influence of transition metal coordination,” *J. Phys. Chem. C* **117**, 25926-25932 (2013).

<sup>9</sup>Y. Dou, Y. Xie, X. Hao, T. Xia, Q. Li, J. Wang, L. Huo, and H. Zhao, “Addressing electrocatalytic activity and stability of LnBaCo<sub>2</sub>O<sub>5+δ</sub> perovskites for hydrogen evolution reaction by structural and electronic features,” *Appl. Catal. B Environ.* **297**, 120403 (2021).

<sup>10</sup>D. Guan, J. Zhou, Z. Hu, W. Zhou, X. Xu, Y. Zhong, B. Liu, Y. Chen, M. Xu, H.J. Lin, C.T. Chen, J. Wang, and Z. Shao, “Searching general sufficient-and-necessary conditions for ultrafast hydrogen-evolving electrocatalysis,” *Adv. Funct. Mater.* **29**, 1900704 (2019).

<sup>11</sup>D. Guan, J. Zhou, Y.C. Huang, C.L. Dong, J.Q. Wang, W. Zhou, and Z. Shao,

“Screening highly active perovskites for hydrogen-evolving reaction via unifying ionic electronegativity descriptor,” *Nat. Commun.* **10**, 3755 (2019).

<sup>12</sup>J. Suntivich, H.A. Gasteiger, N. Yabuuchi, H. Nakanishi, J.B. Goodenough, and Y. Shao-Horn, “Design principles for oxygen-reduction activity on perovskite oxide catalysts for fuel cells and metal-air batteries,” *Nat. Chem.* **3**, 546-550 (2011).

<sup>13</sup>S. Zhou, X. Miao, X. Zhao, C. Ma, Y. Qiu, Z. Hu, J. Zhao, L. Shi, and J. Zeng, “Engineering electrocatalytic activity in nanosized perovskite cobaltite through surface spin-state transition,” *Nat. Commun.* **7**, 11510 (2016).

<sup>14</sup>A. Grimaud, K.J. May, C.E. Carlton, Y.L. Lee, M. Risch, W.T. Hong, J. Zhou, and Y. Shao-Horn, “Double perovskites as a family of highly active catalysts for oxygen evolution in alkaline solution,” *Nat. Commun.* **4**, 2439 (2013).

<sup>15</sup>X. Cheng, E. Fabbri, M. Nachtegaal, I.E. Castelli, M. El Kazzi, R. Haumont, N. Marzari, and T.J. Schmidt, “Oxygen evolution reaction on  $\text{La}_{1-x}\text{Sr}_x\text{CoO}_3$  perovskites: a combined experimental and theoretical study of their structural, electronic, and electrochemical properties,” *Chem. Mater.* **27**, 7662-7672 (2015).

<sup>16</sup>W.T. Hong, K.A. Stoerzinger, Y.-L. Lee, L. Giordano, A. Grimaud, A.M. Johnson, J. Hwang, E.J. Crumlin, W. Yang, and Y. Shao-Horn, “Charge-transfer-energy-dependent oxygen evolution reaction mechanisms for perovskite oxides,” *Energy Environ. Sci.* **10**, 2190-2200 (2017).

<sup>17</sup>X. Li, Y. Bai, and Z. Cheng, “Revealing the correlation of OER with magnetism: a new descriptor of Curie/Neel temperature for magnetic electrocatalysts,” *Adv. Sci.* **8**, 2101000 (2021).

- <sup>18</sup>X. Cheng, E. Fabbri, Y. Yamashita, I.E. Castelli, B. Kim, M. Uchida, R. Haumont, I. Puente-Orench, and T.J. Schmidt, “Oxygen evolution reaction on perovskites: a multi-effect descriptor study combining experimental and theoretical methods,” *ACS Catal.* **8**, 9567-9578 (2018).
- <sup>19</sup>H. Zhang, D. Guan, Z. Hu, Y.-C. Huang, X. Wu, J. Dai, C.-L. Dong, X. Xu, H.-J. Lin, C.-T. Chen, W. Zhou, and Z. Shao, “Exceptional lattice-oxygen participation on artificially controllable electrochemistry-induced crystalline-amorphous phase to boost oxygen-evolving performance,” *Appl. Catal. B Environ.* **297**, 120484 (2021).
- <sup>20</sup>F. Podjaski, D. Weber, S. Zhang, L. Diehl, R. Eger, V. Duppel, E. Alarcón-Lladó, G. Richter, F. Haase, A. Fontcuberta i Morral, C. Scheu, and B.V. Lotsch, “Rational strain engineering in delafossite oxides for highly efficient hydrogen evolution catalysis in acidic media,” *Nat. Catal.* **3**, 55-63 (2019).
- <sup>21</sup>R.P. Forslund, W.G. Hardin, X. Rong, A.M. Abakumov, D. Filimonov, C.T. Alexander, J.T. Mefford, H. Iyer, A.M. Kolpak, K.P. Johnston, and K.J. Stevenson, “Exceptional electrocatalytic oxygen evolution via tunable charge transfer interactions in  $\text{La}_{0.5}\text{Sr}_{1.5}\text{Ni}_{1-x}\text{Fe}_x\text{O}_{4+\delta}$  Ruddlesden-Popper oxides,” *Nat. Commun.* **9**, 3150 (2018).
- <sup>22</sup>Y. Zhu, H.A. Tahini, Z. Hu, Y. Yin, Q. Lin, H. Sun, Y. Zhong, Y. Chen, F. Zhang, H.J. Lin, C.T. Chen, W. Zhou, X. Zhang, S.C. Smith, Z. Shao, and H. Wang, “Boosting oxygen evolution reaction by activation of lattice-oxygen sites in layered Ruddlesden-Popper oxide,” *EcoMat* **2**, e12021 (2020).
- <sup>23</sup>N.I. Kim, Y.J. Sa, T.S. Yoo, S.R. Choi, R.A. Afzal, T. Choi, Y.S. Seo, K.S. Lee, J.Y. Hwang, W.S. Choi, S.H. Joo, and J.Y. Park, “Oxygen-deficient triple perovskites as

highly active and durable bifunctional electrocatalysts for oxygen electrode reactions,” *Sci. Adv.* **4**, eaap9360 (2018).

<sup>24</sup>S. Liu, H. Luo, Y. Li, Q. Liu, and J.L. Luo, “Structure-engineered electrocatalyst enables highly active and stable oxygen evolution reaction over layered perovskite  $\text{LaSr}_3\text{Co}_{1.5}\text{Fe}_{1.5}\text{O}_{10-\delta}$ ,” *Nano Energy* **40**, 115-121 (2017).

<sup>25</sup>S. Yagi, I. Yamada, H. Tsukasaki, A. Seno, M. Murakami, H. Fujii, H. Chen, N. Umezawa, H. Abe, N. Nishiyama, and S. Mori, “Covalency-reinforced oxygen evolution reaction catalyst,” *Nat. Commun.* **6**, 8249 (2015).

<sup>26</sup>Y. Zhu, H.A. Tahini, Z. Hu, Z.G. Chen, W. Zhou, A.C. Komarek, Q. Lin, H.J. Lin, C.T. Chen, Y. Zhong, M.T. Fernandez-Diaz, S.C. Smith, H. Wang, M. Liu, and Z. Shao, “Boosting oxygen evolution reaction by creating both metal ion and lattice-oxygen active sites in a complex oxide,” *Adv. Mater.* **32**, 1905025 (2019).

<sup>27</sup>H. Wang, S. Xu, C. Tsai, Y. Li, C. Liu, J. Zhao, Y. Liu, H. Yuan, F. Abild-Pedersen, F.B. Prinz, J.K. Nørskov, and Y. Cui, “Direct and continuous strain control of catalysts with tunable battery electrode materials,” *Science* **354**, 1031-1036 (2016).

<sup>28</sup>L. Bu, N. Zhang, S. Guo, X. Zhang, J. Li, J. Yao, T. Wu, G. Lu, J.-Y. Ma, D. Su, and X. Huang, “Biaxially strained PtPb/Pt core/shell nanoplate boosts oxygen reduction catalysis,” *Science* **354**, 1410-1414 (2016).

<sup>29</sup>T. Ling, D.Y. Yan, H. Wang, Y. Jiao, Z. Hu, Y. Zheng, L. Zheng, J. Mao, H. Liu, X.W. Du, M. Jaroniec, and S.Z. Qiao, “Activating cobalt(II) oxide nanorods for efficient electrocatalysis by strain engineering,” *Nat. Commun.* **8**, 1509 (2017).

<sup>30</sup>L. Sun, Z. Dai, L. Zhong, Y. Zhao, Y. Cheng, S. Chong, G. Chen, C. Yan, X. Zhang,

H. Tan, L. Zhang, K.N. Dinh, S. Li, F. Ma, and Q. Yan, "Lattice strain and atomic replacement of  $\text{CoO}_6$  octahedra in layered sodium cobalt oxide for boosted water oxidation electrocatalysis," *Appl. Catal. B Environ.* **297**, 120477 (2021).

<sup>31</sup>D. Zhou, S. Wang, Y. Jia, X. Xiong, H. Yang, S. Liu, J. Tang, J. Zhang, D. Liu, L. Zheng, Y. Kuang, X. Sun, and B. Liu, "NiFe hydroxide lattice tensile strain: enhancement of adsorption of oxygenated intermediates for efficient water oxidation catalysis," *Angew. Chem. Int. Ed.* **58**, 736-740 (2019).

<sup>32</sup>J. Hwang, Z. Feng, N. Charles, X.R. Wang, D. Lee, K.A. Stoerzinger, S. Muy, R.R. Rao, D. Lee, R. Jacobs, D. Morgan, and Y. Shao-Horn, "Tuning perovskite oxides by strain: electronic structure, properties, and functions in (electro)catalysis and ferroelectricity," *Mater. Today* **31**, 100-118 (2019).

<sup>33</sup>K.A. Stoerzinger, W.S. Choi, H. Jeon, H.N. Lee, and Y. Shao-Horn, "Role of strain and conductivity in oxygen electrocatalysis on  $\text{LaCoO}_3$  thin films," *J. Phys. Chem. Lett.* **6**, 487-492 (2015).

<sup>34</sup>K. Boulahya, M. Parras, J.M. González-Calbet, U. Amador, J.L. Martínez, V. Tissen, and M.T. Fernández-Díaz, "Ferromagnetism in  $\text{Ba}_5\text{Co}_5\text{O}_{14}$ : a structural, transport, thermal, and magnetic study," *Phys. Rev. B* **71**, 144402 (2005).

<sup>35</sup>A. Khorsand Zak, W.H. Abd. Majid, M.E. Abrishami, and R. Yousefi, "X-ray analysis of ZnO nanoparticles by Williamson-Hall and size-strain plot methods," *Solid State Sci.* **13**, 251-256 (2011).

<sup>36</sup>Z. Cheng, Y. Xiao, W. Wu, X. Zhang, Q. Fu, Y. Zhao, and L. Qu, "All-pH-tolerant in-plane heterostructures for efficient hydrogen evolution reaction," *ACS Nano* **15**, 11417-

11427 (2021).

<sup>37</sup>J. Huang, H. Wang, Z. Qi, P. Lu, D. Zhang, B. Zhang, Z. He, and H. Wang, “Multifunctional metal-oxide nanocomposite thin film with plasmonic Au nanopillars embedded in magnetic  $\text{La}_{0.67}\text{Sr}_{0.33}\text{MnO}_3$  matrix,” *Nano Lett.* **21**, 1032-1039 (2021).

<sup>38</sup>S. Xue, G. Chen, F. Li, Y. Zhao, Q. Zeng, J. Peng, F. Shi, W. Zhang, Y. Wang, J. Wu, and R. Che, “Understanding of strain-induced electronic structure changes in metal-based electrocatalysts: using Pd@Pt core-shell nanocrystals as an ideal platform,” *Small* **17**, 2100559 (2021).

<sup>39</sup>D. Guan, G. Ryu, Z. Hu, J. Zhou, C.-L. Dong, Y.-C. Huang, K. Zhang, Y. Zhong, A.C. Komarek, M. Zhu, X. Wu, C.-W. Pao, C.-K. Chang, H.-J. Lin, C.-T. Chen, W. Zhou, and Z. Shao, “Utilizing ion leaching effects for achieving high oxygen-evolving performance on hybrid nanocomposite with self-optimized behaviors,” *Nat. Commun.* **11**, 3376 (2020).

<sup>40</sup>T. Young, “An essay on the cohesion of fluids,” *Philos. Trans. R. Soc. Lond.* **95**, 65-87 (1805).

<sup>41</sup>S. She, Y. Zhu, H.A. Tahini, Z. Hu, S.-C. Weng, X. Wu, Y. Chen, D. Guan, Y. Song, J. Dai, S.C. Smith, H. Wang, W. Zhou, and Z. Shao, “A molecular-level strategy to boost the mass transport of perovskite electrocatalyst for enhanced oxygen evolution,” *Appl. Phys. Rev.* **8**, 011407 (2021).

<sup>42</sup>Y. Song, J. Liu, Y. Wang, D. Guan, A. Seong, M. Liang, M.J. Robson, X. Xiong, Z. Zhang, G. Kim, Z. Shao, and F. Ciucci, “Nanocomposites: a new opportunity for developing highly active and durable bifunctional air electrodes for reversible protonic

ceramic cells,” *Adv. Energy Mater.* **11**, 2101899 (2021).

<sup>43</sup>M. Risch, A. Grimaud, K.J. May, K.A. Stoerzinger, T.J. Chen, A.N. Mansour, and Y. Shao-Horn, “Structural changes of cobalt-based perovskites upon water oxidation investigated by EXAFS,” *J. Phys. Chem. C* **117**, 8628-8635 (2013).

<sup>44</sup>M. Zhu, D. Guan, Z. Hu, H.-J. Lin, C.-T. Chen, H.-S. Sheu, S. Wang, J. Zhou, W. Zhou, and Z. Shao, “Synergistic effects in ordered Co oxides for boosting catalytic activity in advanced oxidation processes,” *Appl. Catal. B Environ.* **297**, 120463 (2021).

<sup>45</sup>J.M. Chen, Y.Y. Chin, M. Valldor, Z. Hu, J.M. Lee, S.C. Haw, N. Hiraoka, H. Ishii, C.W. Pao, K.D. Tsuei, J.F. Lee, H.J. Lin, L.Y. Jang, A. Tanaka, C.T. Chen, and L.H. Tjeng, “A complete high-to-low spin state transition of trivalent cobalt ion in octahedral symmetry in  $\text{SrCo}_{0.5}\text{Ru}_{0.5}\text{O}_{3-\delta}$ ,” *J. Am. Chem. Soc.* **136**, 1514-1519 (2014).

<sup>46</sup>J. Zhou, L. Zhang, Y.C. Huang, C.L. Dong, H.J. Lin, C.T. Chen, L.H. Tjeng, and Z. Hu, “Voltage- and time-dependent valence state transition in cobalt oxide catalysts during the oxygen evolution reaction,” *Nat. Commun.* **11**, 1984 (2020).

<sup>47</sup>Y.Y. Chin, Z. Hu, H.J. Lin, S. Agrestini, J. Weinen, C. Martin, S. Hébert, A. Maignan, A. Tanaka, J.C. Cezar, N.B. Brookes, Y.F. Liao, K.D. Tsuei, C.T. Chen, D.I. Khomskii, and L.H. Tjeng, “Spin-orbit coupling and crystal-field distortions for a low-spin  $3d^5$  state in  $\text{BaCoO}_3$ ,” *Phys. Rev. B* **100**, 205139 (2019).

<sup>48</sup>N. Hollmann, Z. Hu, M. Valldor, A. Maignan, A. Tanaka, H.H. Hsieh, H.J. Lin, C.T. Chen, and L.H. Tjeng, “Electronic and magnetic properties of the kagome systems  $\text{YBaCo}_4\text{O}_7$  and  $\text{YBaCo}_3\text{MO}_7$  ( $M=\text{Al}, \text{Fe}$ ),” *Phys. Rev. B* **80**, 085111 (2009).

<sup>49</sup>T. Burnus, Z. Hu, H. Wu, J.C. Cezar, S. Niitaka, H. Takagi, C.F. Chang, N.B. Brookes,

H.J. Lin, L.Y. Jang, A. Tanaka, K.S. Liang, C.T. Chen, and L.H. Tjeng, “X-ray absorption and x-ray magnetic dichroism study on  $\text{Ca}_3\text{CoRhO}_6$  and  $\text{Ca}_3\text{FeRhO}_6$ ,” *Phys. Rev. B* **77**, 205111 (2008).

<sup>50</sup>Z. Hu, C. Grazioli, M. Knupfer, M.S. Golden, J. Fink, P. Mahadevan, A. Kumar, S. Ray, D.D. Sarma, S.A. Warda, D. Reinen, S. Kawasaki, M. Takano, C. Schussler-Langeheine, C. Mazumdar, and G. Kaindl, “Difference in spin state and covalence between  $\text{La}_{1-x}\text{Sr}_x\text{CoO}_3$  and  $\text{La}_{2-x}\text{Sr}_x\text{Li}_{0.5}\text{Co}_{0.5}\text{O}_4$ ,” *J. Alloys Compd.* **343**, 5-13 (2002).

<sup>51</sup>Z. Liu, Y. Sakai, J. Yang, W. Li, Y. Liu, X. Ye, S. Qin, J. Chen, S. Agrestini, K. Chen, S.C. Liao, S.C. Haw, F. Baudalet, H. Ishii, T. Nishikubo, H. Ishizaki, T. Yamamoto, Z. Pan, M. Fukuda, K. Ohashi, K. Matsuno, A. Machida, T. Watanuki, S.I. Kawaguchi, A.M. Arevalo-Lopez, C. Jin, Z. Hu, J.P. Attfield, M. Azuma, and Y. Long, “Sequential spin state transition and intermetallic charge transfer in  $\text{PbCoO}_3$ ,” *J. Am. Chem. Soc.* **142**, 5731-5741 (2020).

<sup>52</sup>S. Agrestini, K. Chen, C.Y. Kuo, L. Zhao, H.J. Lin, C.T. Chen, A. Rogalev, P. Ohresser, T.S. Chan, S.C. Weng, G. Auffermann, A. Völzke, A.C. Komarek, K. Yamaura, M.W. Haverkort, Z. Hu, and L.H. Tjeng, “Nature of the magnetism of iridium in the double perovskite  $\text{Sr}_2\text{CoIrO}_6$ ,” *Phys. Rev. B* **100**, 014443 (2019).

<sup>53</sup>A. Juhin, F. de Groot, G. Vankó, M. Calandra, and C. Brouder, “Angular dependence of core hole screening in  $\text{LiCoO}_2$ : a DFT+ $U$  calculation of the oxygen and cobalt  $K$ -edge x-ray absorption spectra,” *Phys. Rev. B* **81**, 115115 (2010).

<sup>54</sup>Y. Wang, W. Tian, J. Wan, W. Fu, H. Zhang, Y. Li, and Y. Wang, “Probing the origin of group VB transition metal monocarbides for high-efficiency hydrogen evolution

reaction: a DFT study,” *Appl. Surf. Sci.* **539**, 148312 (2021).

<sup>55</sup>J.C. Liu, X.L. Ma, Y. Li, Y.G. Wang, H. Xiao, and J. Li, “Heterogeneous Fe<sub>3</sub> single-cluster catalyst for ammonia synthesis via an associative mechanism,” *Nat. Commun.* **9**, 1610 (2018).

<sup>56</sup>I.V. Chepkasov, M.A. Visotin, E.A. Kovaleva, A.M. Manakhov, V.S. Baidyshev, and Z.I. Popov, “Stability and electronic properties of PtPd nanoparticles via MD and DFT calculations,” *J. Phys. Chem. C* **122**, 18070-18076 (2018).

<sup>57</sup>S. Zhang, Z.Q. Huang, Y. Ma, W. Gao, J. Li, F. Cao, L. Li, C.R. Chang, and Y. Qu, “Solid frustrated-Lewis-pair catalysts constructed by regulations on surface defects of porous nanorods of CeO<sub>2</sub>,” *Nat. Commun.* **8**, 15266 (2017).

<sup>58</sup>Z. Qu, F. Sun, X. Liu, J. Gao, Z. Qie, and G. Zhao, “The effect of nitrogen-containing functional groups on SO<sub>2</sub> adsorption on carbon surface: enhanced physical adsorption interactions,” *Surf. Sci.* **677**, 78-82 (2018).

<sup>59</sup>B. Ravel, and M. Newville, “ATHENA, ARTEMIS, HEPHAESTUS: data analysis for X-ray absorption spectroscopy using IFEFFIT,” *J. Synchrotron Rad.* **12**, 537-541 (2005).

<sup>60</sup>V.I. Anisimov, F. Aryasetiawan, and A.I. Lichtenstein, “First-principles calculations of the electronic structure and spectra of strongly correlated systems: the LDA + U method,” *J. Phys.: Condens. Matter* **9**, 767-808 (1997).

<sup>61</sup>B. Hammer, L.B. Hansen, and J.K. Nørskov, “Improved adsorption energetics within density-functional theory using revised Perdew-Burke-Ernzerhof functionals,” *Phys. Rev. B* **59**, 7413-7421 (1999).

<sup>62</sup>J.P. Perdew, K. Burke, and M. Ernzerhof, “Generalized gradient approximation made

simple,” Phys. Rev. Lett. **77**, 3865-3868 (1996).

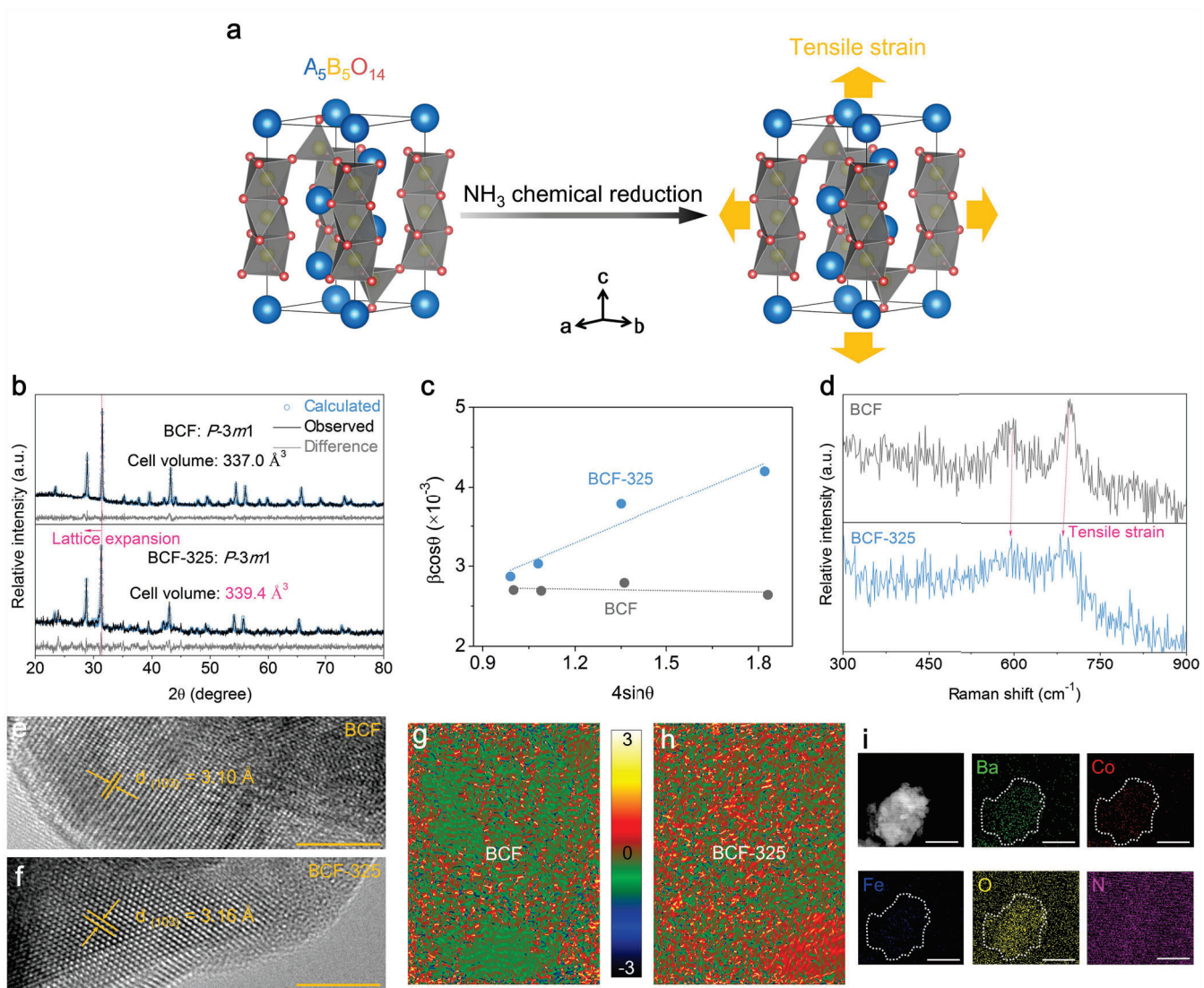
<sup>63</sup>P.E. Blöchl, “Projector augmented-wave method,” Phys. Rev. B **50**, 17953-17979 (1994).

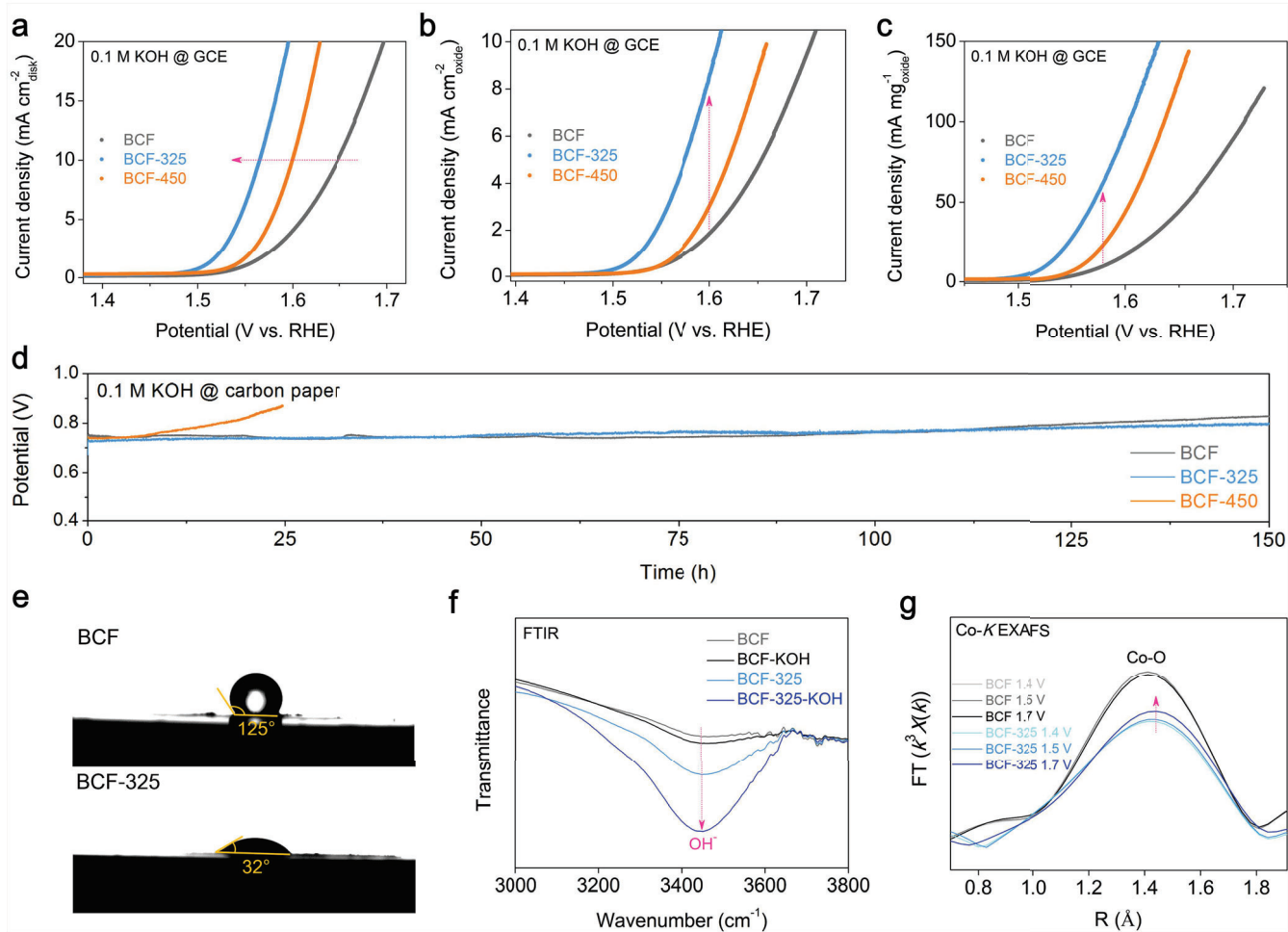
<sup>64</sup>M. Bajdich, M. García-Mota, A. Vojvodic, J.K. Nørskov, and A.T. Bell, “Theoretical investigation of the activity of cobalt oxides for the electrochemical oxidation of water,” J. Am. Chem. Soc. **135**, 13521-13530 (2013).

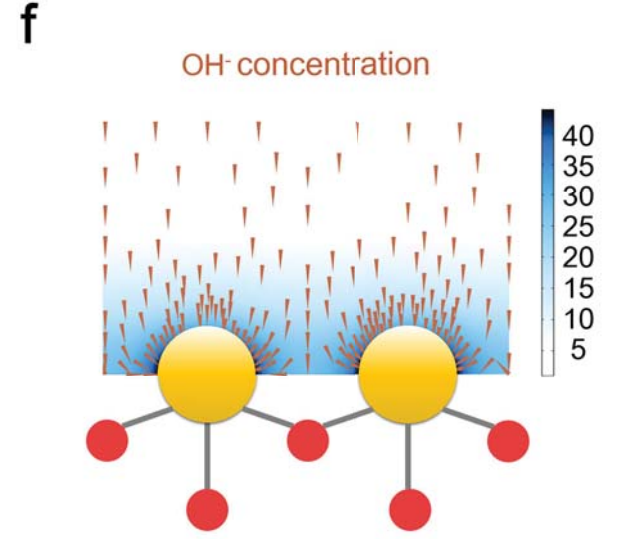
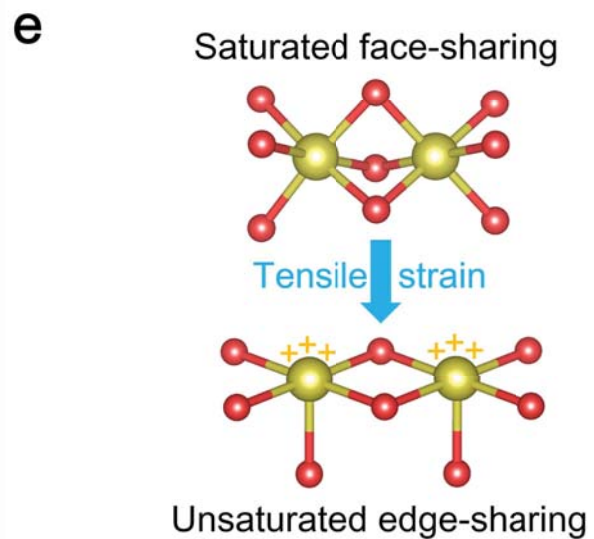
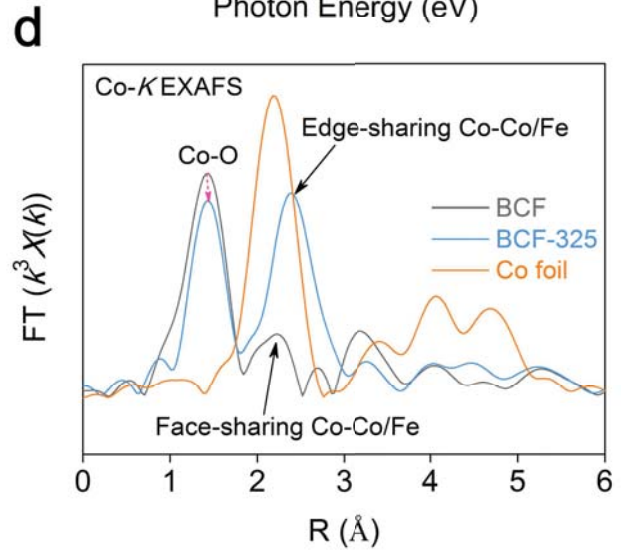
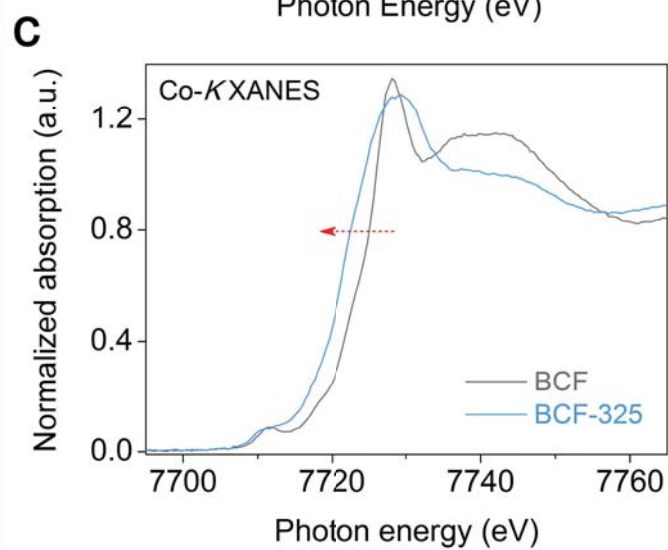
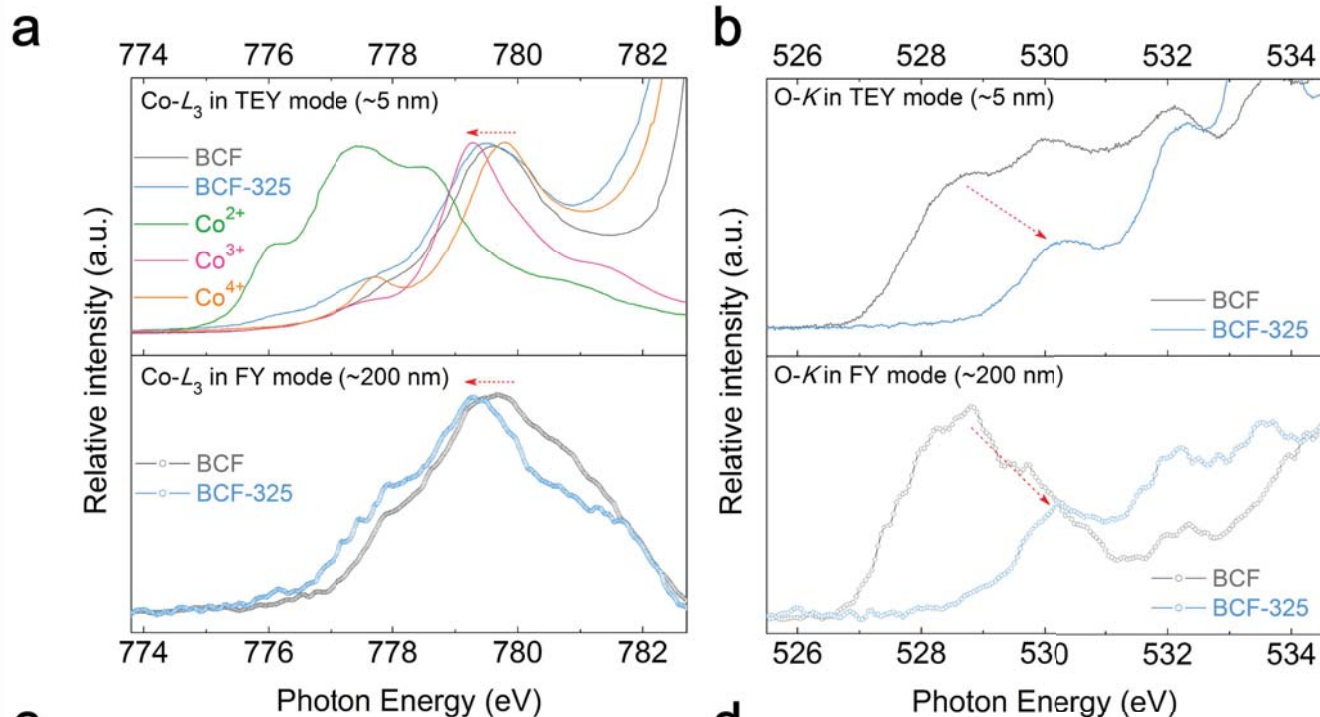
<sup>65</sup>S. Grimme, S. Ehrlich, and L. Goerigk, “Effect of the damping function in dispersion corrected density functional theory,” J. Comput. Chem. **32**, 1456-1465 (2011).

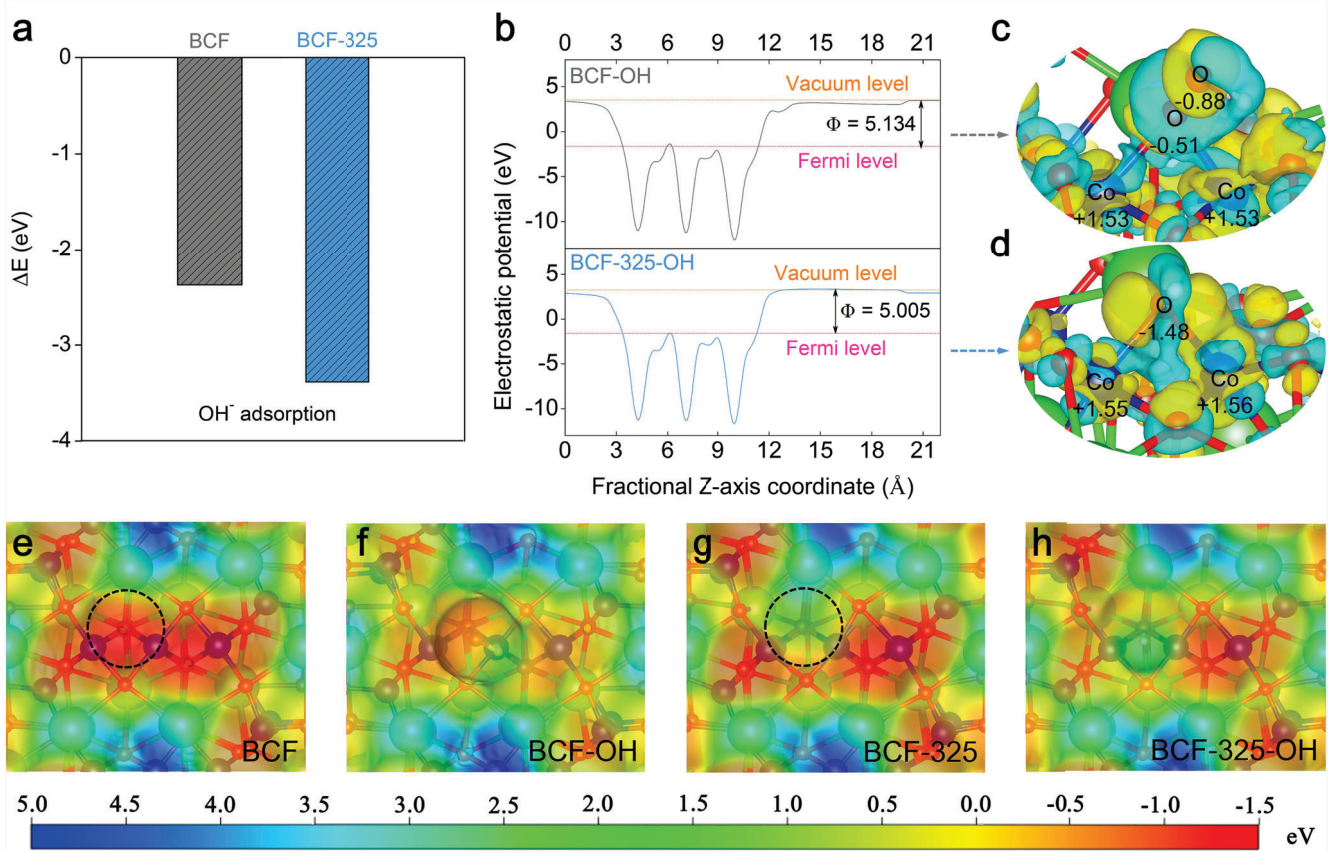
<sup>66</sup>S. Grimme, J. Antony, S. Ehrlich, and H. Krieg, “A consistent and accurate *ab initio* parametrization of density functional dispersion correction (DFT-D) for the 94 elements H-Pu,” J. Chem. Phys. **132**, 154104 (2010).

<sup>67</sup>J. Neugebauer, and M. Scheffler, “Adsorbate-substrate and adsorbate-adsorbate interactions of Na and K adlayers on Al(111),” Phys. Rev. B **46**, 16067-16080 (1992).









Introducing tensile strain:

